Nanoscale

PAPER

View Article Online
View Journal

Cite this: DOI: 10.1039/d6nr00068a

Boosting the NIR-I luminescence of lanthanide nanoparticles excited in NIR-II by plasmonic arrays

Jiamin Xu,[a] Fu Ming,[b] Yunfan Xu,[a] Jingdong Xu,[a] Xiaofei Xiao,[a] Qiyu Zhang,[a] Yao Lu,[a] Koen Evers,[a] Changxu Liu,[b] Stefan Maier,[c] Rupert Oulton,[a] Mary Ryan[a] and Fang Xie *[a]

The exploitation of lanthanide-induced NIR luminescence holds significant potential for advancing biosensing and imaging technologies because of its deeper imaging penetration depth and lower biosensing noise than visible light. However, the low quantum efficiency of light generation, along with the high cost and poor sensitivity of light detection for NIR-II photons, have largely constrained the application of NIR-II luminescence for bio-imaging and sensing. To overcome these challenges, we have developed a new strategy for NIR bioimaging and sensing by using Tm^{3+}-doped $NaYF_4$ upconversion nanoparticles (UCNPs) that emit NIR-I upconversion luminescence (UCL) at 808 nm under NIR-II excitation at 1208 nm. The 1208 nm excitation enables deeper imaging penetration due to negligible autofluorescence, thereby reducing biosensing noise, resulting in an enhanced signal-to-noise ratio (S/N) from a minimal noise background. Meanwhile, the NIR-I emission at 808 nm allows deep tissue penetration, while allowing highly sensitive detection of NIR-I photons using conventional detectors, which are much more accessible than NIR-II detection systems. The intrinsically weak NIR UCL signals were further amplified by up to 210-fold using a pioneering plasmonic approach, achieved by coupling UCNPs with periodic silver hole–cap nanoarrays (Ag-HCNAs). Three-dimensional finite-difference time-domain (3D-FDTD) simulations and lifetime analyses revealed substantial electric field enhancements under 1208 nm excitation and accelerated radiative decay at 808 nm, contributing to both excitation and emission enhancement. The potential use of Ag-HCNA–UCNP conjugates for fluorescence immunoassay platforms was further validated by immobilizing streptavidin-functionalized UCNPs (SA-UCNPs) onto biotinylated Bovine Serum Albumin (bBSA) pre-grafted substrates, resulting in up to a 113-fold increase in UCL intensity. This plasmonic-enhanced UCL platform offers significant advantages, including cost-effective detection of 808 nm emission using silicon-based detectors, an improved signal-to-noise ratio through enhanced tissue penetration, and reduced autofluorescence enabled by NIR-II excitation.

Received 6th January 2026,
Accepted 30th March 2026

DOI: 10.1039/d6nr00068a

rsc.li/nanoscale

Introduction

Fluorescence-based technologies within the visible (400–700 nm) and the first near-infrared (NIR-I, 700–900 nm) regions have been extensively explored for biomedical applications over the past few decades.[1–3] However, these spectral regions suffer from significant limitations due to photon absorption by biological media, such as water, haemoglobin, lipids, and melanin, as well as substantial photon scattering within biological tissues, leading to severe interference from biological tissue autofluorescence in the visible range.[4,5] Although NIR-I wavelengths partially mitigate these issues by reducing autofluorescence and enabling deeper tissue penetration, further improvements are required for high-performance biomedical applications.[6,7]

In contrast, the second near-infrared window (NIR-II, 1000–1700 nm) exhibits outstanding capabilities, including deeper tissue penetration, minimal tissue scattering, negligible autofluorescence, and superior temporal and spatial resolution.[8,9] To fully harness the potential of NIR-II fluorescence for advanced biomedical imaging and biosensing, the development of efficient and stable fluorescent nanoprobes is essential.

Among the available nanoprobes such as small-molecule dyes,[10,11] quantum dots (QDs)[12,13] and single-walled carbon nanotubes (SWCNTs),[14,15] lanthanide-doped nanoparticles (LDNPs) have attracted particular interest due to their unique luminescence properties.[16,17] These include large Stokes or anti-Stokes shifts, robust photostability, long luminescence

[a]Imperial College London, London, UK. E-mail: f.xie@imperial.ac.uk
[b]University of Exeter, Exeter, UK
[c]Monash University, Clayton, Australia

lifetimes, and low cytotoxicity.[17] Such intrinsic characteristics render LDNPs promising candidates for a broad range of applications, ranging from *in vitro* bioassays to *in vivo* imaging, positioning them as one of the most promising candidates in the field of nanobiotechnology.[16,18]

LDNPs can emit both upconversion luminescence (UCL) and downconversion luminescence (DCL) according to their luminescence pathways.[19] UCL is an anti-Stokes process.[20,21] This involves the successive absorption of two or more lower-energy photons in the NIR-I/NIR-II regions, followed by the emission of one higher-energy photon, typically in the visible region. In contrast, DCL is a Stokes process, where a photon is absorbed and converted into a photon with lower energy. LDNPs typically consist of a host matrix that incorporates sensitizer and emitter ions such as Yb^{3+}, Er^{3+}, Nd^{3+}, and Tm^{3+}, enabling emission across the visible to NIR-II regions under NIR-II excitation.[18,22] Various host matrix materials with asymmetric crystalline structures have been successful in producing LDNPs with detectable UCL or DCL signals, including fluoride-based hosts[23–25] and oxide-based hosts.[26,27] Among these, fluoride hosts, particularly $NaLnF_4$, are preferred due to their low phonon energies and high photochemical stability, which improve the efficiency of lanthanide-ion-induced luminescence.[28,29] Previous studies have reported various types of UCL-emitting LDNPs, commonly termed upconversion nanoparticles (UCNPs), which are frequently excited in the NIR-II region to maximise tissue penetration.[22,30] However, UCL processes suffer from intrinsically low quantum efficiencies, and their visible emissions are prone to re-absorption by biological tissues, limiting detection sensitivity.[31]

In contrast, a class of LDNPs that emit photons at lower energy than the excitation source is termed downconversion nanoparticles (DCNPs). These are engineered to optimize both excitation and emission wavelengths within the NIR-II region, which can enhance tissue penetration and reduce autofluorescence, making them highly attractive for biological applications. Recent studies have demonstrated that NIR-II emitting DCNPs can overcome key limitations of conventional fluorescence immunoassays by reducing background interference and lowering the limit of detection (LOD).[41–43] Such NIR-II emitting immunoassay nanoplatforms therefore offer enhanced sensitivity and improved accuracy.

Nevertheless, the practical application of LDNPs remains limited by inherently low NIR quantum yields (typically 0.1–3%).[18,22,32] Furthermore, detection of NIR-II photons requires indium gallium arsenide (InGaAs)-based CCD cameras, which are significantly more expensive than conventional Si-based CCD cameras (suitable for NIR-I photons but unsuitable for NIR-II photons). Since NIR-II detectors are deemed too expensive for broad clinical use,[9,33] the high cost of essential instrumentation presents another major barrier to widespread adoption.

To address these limitations, there is a pressing need to develop a new class of LDNPs that combine the advantages of traditional UCNPs and DCNPs. Ideally, such systems would be excited in the NIR-II region and emit in the NIR-I region, enabling deep tissue penetration, low autofluorescence, and detection with cost-effective Si-based CCD cameras, thereby expanding their applications in bioimaging and biosensing. Moreover, the quantum efficiency of these nanoparticles should be enhanced to match or surpass that of commercial fluorophores.

One promising strategy to overcome the low quantum efficiency of LDNPs is metal-enhanced fluorescence (MEF), also known as plasmonic enhanced fluorescence. MEF exploits surface plasmon resonance (SPR) in metallic nanostructures to modify the excitation and emission dynamics of nearby fluorophores, leading to significant fluorescence amplification.[34–36] Periodic noble metal nanoarrays with sharp SPR features have emerged as promising nanoplatforms for MEF.[37,38] Among fabrication approaches, colloidal lithography offers a scalable and cost-effective route to fabricate noble metal periodic nanoarrays, such as gold nanohole arrays,[39] silver nanotriangular arrays,[40] and gold hole–cap arrays.[28] These two-dimensional (2D) and three-dimensional (3D) nanoarray architectures enable precise spectral tuning for optimal plasmonic coupling to amplify the weak emission of LDNPs.

In this work, we report a novel type of $NaYF_4$ UCNP solely doped with Tm^{3+} ions capable of emitting NIR-I photons at 808 nm under 1208 nm NIR-II laser excitation. Upon coupling these UCNPs with Ag hole–cap coupled nanoarrays (Ag-HCNAs), a remarkable enhancement exceeding 210-fold in UCL intensity was achieved. The three-dimensional Ag-HCNAs were fabricated *via* colloidal lithography, as illustrated in Scheme 1, where a self-assembled film of polystyrene (PS) spheres was oxygen plasma-etched to facilitate the deposition of a thin Ag layer not only in the gaps between adjacent oval-shaped PS spheres but also on their upper hemispheres. Furthermore, the applicability of this plasmonic platform for accessible fluorescence immunoassays was validated by immobilizing a sub-monolayer of streptavidin-functionalized UCNPs (SA-UCNPs) on bBSA pre-grafted Ag-HCNA substrates. An enhancement of up to 113-fold relative to glass substrates was obtained, demonstrating the strong potential of this system to significantly amplify weak NIR-UCL signals in plasmonic-enhanced UCL immunoassays used for biosensing.

Experimental section

Chemicals and materials

Sodium hydroxide (NaOH, ≥98%), thulium(III) acetate hydrate (99.9%), yttrium(III) acetate hydrate (99.9%), ammonium fluoride (NH_4F, 96%), cyclohexane (99.5%), oleic acid (OA, 90%), 1-octadecene (ODE, 90%), poly(acrylic acid) (PAA), methanol (≥99.9%), silicon wafers, sodium dodecyl sulfate (SDS, >99.0%), phosphate buffered saline (PBS), streptavidin (from *Streptomyces avidinii*, affinity purified), 1-ethyl-3-(3-dimethylaminopropyl)carbodiimide, *N*-hydroxysuccinimide (NHS), phosphate buffered saline (PBS, pH 7.4) and biotinylated bovine serum albumin (bBSA) were purchased from Sigma-Aldrich. Thiol-PEG-amine HCl salt (SH-PEG7500-NH_2, MW:

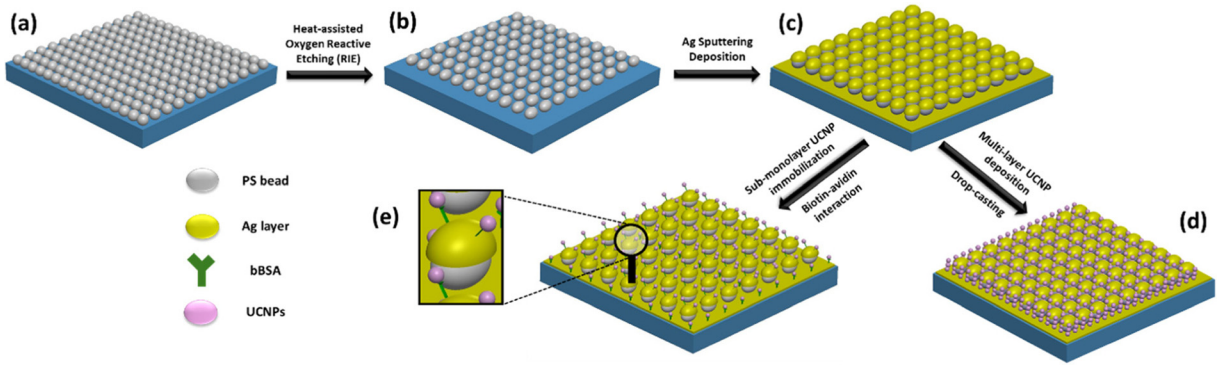

Scheme 1 Schematic illustration of the workflow for plasmonic-enhanced UCL on Ag-HCNA films: (a) self-assembled PS beads on the glass substrate, (b) formation of self-assembled shrunk PS beads *via* RIE, (c) creation of the Ag-HCNA film through Ag sputtering, (d) deposition of multi-layer Tm^{3+}-doped UCNPs onto Ag-HCNAs *via* drop-casting, and (e) immobilization of a sub-monolayer of DCNPs onto the Ag-HCNA film through biotin–avidin interaction.

7500) was bought from JenKem Technology, Texas, USA. Monodisperse polystyrene solution (5% w/v, 617 nm, and 418 nm) was purchased from Bangs Laboratories. All the chemicals were used without further purification.

Synthesis of Tm^{3+}-doped NaYF4 upconversion nanocrystals (UCNPs)

Following a typical solvothermal method,[23] 0.05 mmol of thulium(III) acetate hydrate and 0.95 mmol of yttrium(III) acetate hydrate powders were mixed in a three-neck round bottom flask. To this mixture, 7.5 ml of OA and 15 ml of ODE were then added with vigorous stirring. The mixture was heated to 145 °C and maintained at this temperature for 1 h under vacuum until a transparent faint-yellow solution was obtained. After cooling the solution to 40 °C, a mixture of 4 mmol of NH_4F and 2.5 mmol of NaOH dissolved in 10 ml of methanol was added. The resulting turbid solution was stirred vigorously at a temperature below 50 °C for 30 min, followed by heating up to 120 °C under vacuum to remove excessive water and methanol. Once no bubbles were observed, the orange solution was heated to 300 °C under an argon atmosphere and maintained at this temperature for 90 min. After the completion of the reaction, the solution was cooled to room temperature, and excess chemicals were washed several times with ethanol and acetone. The resulting pellet was finally redispersed in cyclohexane. Tm^3-doped $NaYF_4$ UCNPs with various Tm^{3+} doping concentrations were prepared by adjusting the molar ratio between thulium(III) acetate hydrate and yttrium(III) acetate, while keeping all other steps constant.

Preparation of PAA-functionalized UCNPs (PAA-UCNPs)

The oleate ligands on the surface of DCNPs were initially eliminated through acid treatment.[44] Briefly, the cyclohexane-dispersed DCNPs were centrifuged and the collected yellow pellet was re-dispersed in 15 ml of ethanol, followed by adding 0.5 ml of HCl (0.1 M) to adjust the solution pH to around 4. The turbid mixture was sonicated for 30 min at 40 °C, followed by stirring at room temperature for 12 h. The obtained product was centrifuged and washed with water until the pH was neutral. To conjugate PAA onto the UCNPs, 2 mg ml^{-1} of PAA powder was added to 10 ml of aqueous UCNP solution. With rigorous stirring, NaOH (1 M) solution was slowly dropped into the solution until the pH was 10–11. The solution was stirred at room temperature for 12 h. The obtained nanoparticles were collected by centrifugation at 10 000 rpm for 15 minutes, washed multiple times with ethanol and water, and then redispersed in 10 ml of water. Finally, the nanoparticles were stored in a refrigerator at 4 °C until use.

Streptavidin conjugation with PAA-UCNPs

Conjugation of streptavidin with PAA-UCNPs was achieved through EDC–NHS chemistry, following the reported method.[45] Briefly, PAA-UCNPs in 1 ml of MES buffer (50 mM, pH 6.0) were added to 0.4 mg of EDC and 0.6 mg of NHS. The solution was incubated on an orbital shaker for 30 min. After the reaction was complete, the solution was centrifuged at 10 000 rpm for 30 min and the supernatant was discarded. The activated PAA-UCNPs were re-dispersed in 1 ml of PBS buffer (pH 7.4) containing 100 μg ml^{-1} of streptavidin. The solution was then vortexed at room temperature for 4 h. The streptavidin-conjugated UCNPs were collected by centrifugation at 4000 rpm for 20 min at 4 °C and re-dispersed in 1 ml of PBS solution.

Fabrication of Ag-HCNAs

The fabrication of the silver hole–cap nanoarray (Ag-HCNA) film followed a typical colloidal lithography method.[28] Initially, two types of polystyrene sphere (PS418 and PS617) formed their respective monolayer of closely-packed PS spheres in a hexagonal arrangement on glass slides through a previously reported self-assembly technique.[46,47] The monolayer of PS spheres on the glass slide was treated with reactive ion etching (RIE) using O_2 for 50 s for PS418 and 40 s for PS617, respectively, with the same O_2 pressure of 20 Pa and O_2

flow rate of 20 sccm. Afterwards, a 40 nm thick layer of Ag was sputtered onto the etched PS sphere substrate using a Hex deposition system, with an argon flow rate of 10 sccm, a voltage of 630 V, and a current of 100 mA. The obtained substrate was placed on a hot plate at 90 °C for 2 min and stored in a desiccator covered with aluminium foil until use.

Deposition of multilayered UCNPs onto Ag-HCNAs

10 μl of SH-PEG7500-NH_2 in ethanol (10 μg ml^{-1}) was dropped onto both types of Ag-HCNA films, followed by incubating under humidity conditions for 30 min. The excess SH-PEG7500-NH_2 was rinsed off with ethanol. The as-prepared PAA-DCNP solution was diluted to around 50 μg ml^{-1}, followed by depositing 9 μL of DCNP solution onto the center of each type of PEGylated Ag-HCNA *via* drop-casting. The sample was placed under a fume hood for at least 30 min until the solvent was completely evaporated. As a reference, the same amount of DCNPs was deposited onto a glass slide using the same drop-casting technique.

Immobilization of streptavidin-functionalized UCNPs (SA-UCNPs) onto Ag-HCNAs

The immobilization of SA-UCNPs onto Ag-HCNAs was achieved through a Biotin–avidin interaction.[45,48] Briefly, a solution containing 100 μg ml^{-1} of bBSA in PBS buffer (pH 7.4) was dropped onto the surface of Ag-HCNAs, followed by incubation under a humidified environment for 2 h. The excess bBSA molecules were then removed through rinsing with PBS buffer, and the sample was gently dried using N_2 gas. Subsequently, a solution containing 50 μg ml^{-1} of streptavidin-DCNPs was dropped onto the surface of bBSA-coated Ag-HCNAs, and the sample was incubated under a humidified environment for 2 h. Later, unbound SA-DCNPs were thoroughly rinsed off with PBS buffer, and the obtained SA-DCNP-immobilized Ag-HCNAs were dried using N_2 gas. The fluorescence spectra were immediately recorded.

To assess the number of SA-DCNPs bound to Ag-HCNAs, the fluorescence intensity of unbound nanoparticles was also measured. The number of bound SA-DCNPs was determined by subtracting the fluorescence intensity of the total amount of SA-DCNPs from that of the unbound nanoparticles. As a control, an equivalent amount of SA-DCNPs was deposited onto bBSA-coated glass. The average fluorescence enhancement factor was calculated based on $Enh_{total} = (I_{Ag}/I_{glass})(N_{glass}/N_{Ag})$, where I_{Ag} and I_{glass} represent the UCL intensity from DCNPs immobilized on Ag-HCNAs and glass and N_{Ag} and N_{glass} represent the amount of DCNPs bound to Ag-HCNAs and glass, respectively.

Characterization

The X-ray diffraction (XRD) profiles of UCNPs were obtained using a PANalytical diffractometer with Cu Kα irradiation (k = 1.5406 Å) as the X-ray source, and the measurement spanned a range (2θ) of 10–70° (2θ) with a step size of 0.0167°. The morphological features of UCNPs were characterized using a JEOL 2100F transmission electron microscope (TEM) equipped with Energy-Dispersive X-ray Spectroscopy (EDX, Oxford Instruments, UK) at an accelerating voltage of 200 kV. The substrate samples were characterized using a Zeiss Auriga Scanning electron microscope (SEM) with an InLens detector at an acceleration voltage of 5 kV. The EDX (Oxford Instruments, UK) analysis was performed at 20 kV. The extinction spectra of the samples were obtained using a UV-vis-NIR spectrophotometer (Agilent Cary 5000). For the solution sample, a high-performance quartz cuvette was used, and the measurement was conducted from 700 nm to 1100 nm. The fluorescence intensities of aqueous UCNP samples with different Tm^{3+} doping concentrations were measured using a Fluorolog Tau3 system (Horiba Scientific) equipped with a PMT detector (700–900 nm) and an MDL-1028 nm continuous wave laser (500 mW, Changchun New Industries Optoelectronics Technology Co., Ltd) to optimize the Tm^{3+} concentration. Fluorescence spectra of the substrate samples were obtained using a Princeton Instruments Spec 10 system with an SP2300 equipped with a CW laser diode at a wavelength of 1208 nm. The excitation beam was incident perpendicularly onto the surface of the sample. The lifetimes of Tm^{3+}-doped PAA-UCNPs on glass and Ag-HCNAs were characterized using a frequency domain lifetime measurement technique with modulated pump and detection methodology, while the Purcell factor simulations were conducted using the commercial FDTD software Lumerical. Detailed methods for lifetime measurement and Purcell factor simulation are provided in the SI, and reported in our prior work.[28,49]

Results and discussion

Synthesis of Tm^{3+}-doped NaYF4 UCNPs

Monodispersed $NaYF_4$:5% Tm^{3+} UCNPs capped with oleate ligands were synthesized using a typical solvothermal method, as illustrated in Fig. 1a. This Tm^{3+} concentration was optimized to achieve the highest UCL performance at 808 nm, as shown in SI Fig. S1. The capped oleate ligands are hydrophobic and are not biocompatible, hence a ligand exchange step was performed by acid washing to remove oleate ligands and subsequently functionalized with PAA. Fig. 1b and c show the morphological features of PAA-functionalized UCNPs under different magnification, and it was observed that the size, shape and uniformity of PAA-functionalized UCNPs underwent negligible changes compared to the OA-capped UCNPs. Fig. 1e shows that the as-prepared $NaYF_4$: 5% Tm^{3+} UCNPs possess an average size of 21 ± 3.1 nm with a narrow size distribution. Fig. 1e shows the XRD pattern of PAA-functionalized $NaYF_4$: 5% Tm^{3+} UCNPs deposited onto a Si wafer. It is noted that the two line-like peaks at 33° and 48° denote the characteristic peaks of Si, while the other characteristic peaks are well fitted to the hexagonal $NaYF_4$ crystalline structure indexed by reference 00-028-1192. The lattice spacing of 0.296 nm measured from the HR-TEM image (Fig. 1c) corresponds to the (110) facets of hexagonal $NaYF_4$, showing good alignment with the XRD results.

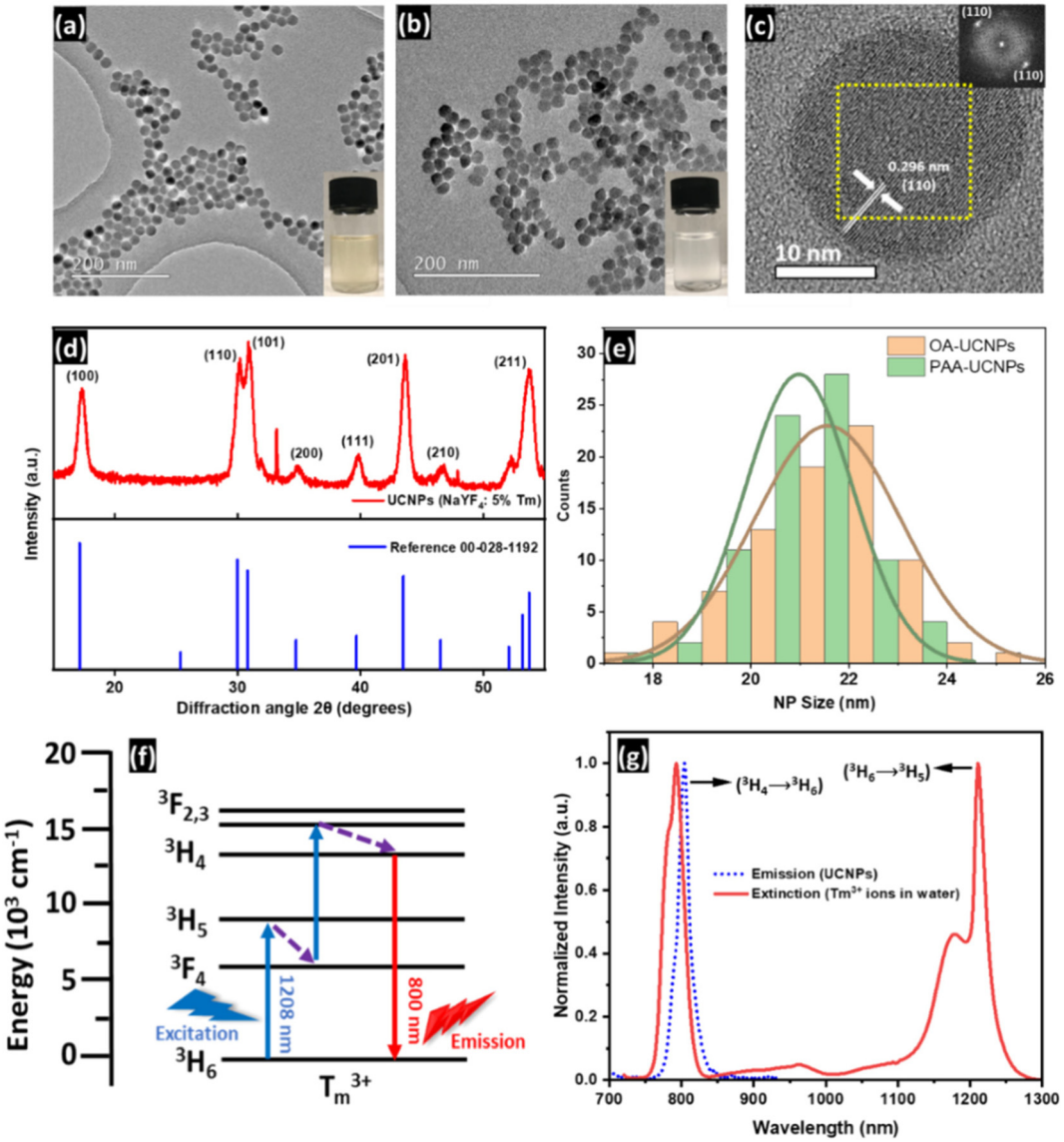

Fig. 1 Characterization of Tm^{3+}-doped $NaYF_4$ UCNPs. TEM images of (a) OA-capped UCNPs and (b) PAA-functionalized UCNPs, and (c) high-resolution TEM image of single PAA-functionalized UCNPs. The insets in (a and b) show digital camera images of OA-capped UCNPs dispersed in cyclohexane and PAA-functionalized UCNPs in water. The inset in (c) shows the FFT pattern of the selected area within the yellow square. (d) XRD pattern of Tm-doped $NaYF_4$ UCNPs dispersed on a wafer (red spectrum) and the reference peaks of 00-028-1192 (blue vertical lines). (e) Statistic size distributions of OA-capped UCNPs and PAA-functionalized UCNPs. (f) Energy transfer diagram of Tm-doped $NaYF_4$ UCNPs under excitation at 1208 nm. (g) Normalized extinction spectrum of Tm^{3+} ions in water (red spectrum) and normalized NIR upconversion emission spectrum of aqueously dispersed Tm-doped $NaYF_4$ UCNPs under excitation at 1208 nm.

Structural design and fabrication of Ag-HCNAs

The morphological features of two types of Ag-HCNA films at different fabrication stages were characterized by SEM, as shown in Fig. 2a–d and SI Fig. S2 and S3. The structural parameters of the films corresponding to each fabrication stage are summarized in SI Table S1. Initially, the unetched PS-617 beads exhibited an average diameter of 617 ± 12 nm and a pitch size of ~610 ± 11 nm in the closely-packed PS film. After 50 s of oxygen plasma etching and subsequent Ag deposition, the PS beads transformed into an oval shape with reduced longitudinal and transverse dimensions of 494 ± 14 nm and 384 ± 8 nm (Fig. S2), respectively, while maintaining a largely unchanged pitch size (SI Fig. S3). The deformation from the spherical shape to an oval shape was induced by temperature gradients during plasma etching, as previously reported.[50] Consequently, the subsequent Ag deposition resulted in Ag hemispherical caps with an average longitudinal diameter of ~530 ± 17 nm, an average separation distance of ~80 ± 7 nm between adjacent caps, and an estimated gap size of ~147 ± 8 nm (Fig. 2a and c). For PS-417 beads with 45 seconds of oxygen plasma etching and subsequent Ag deposition, the

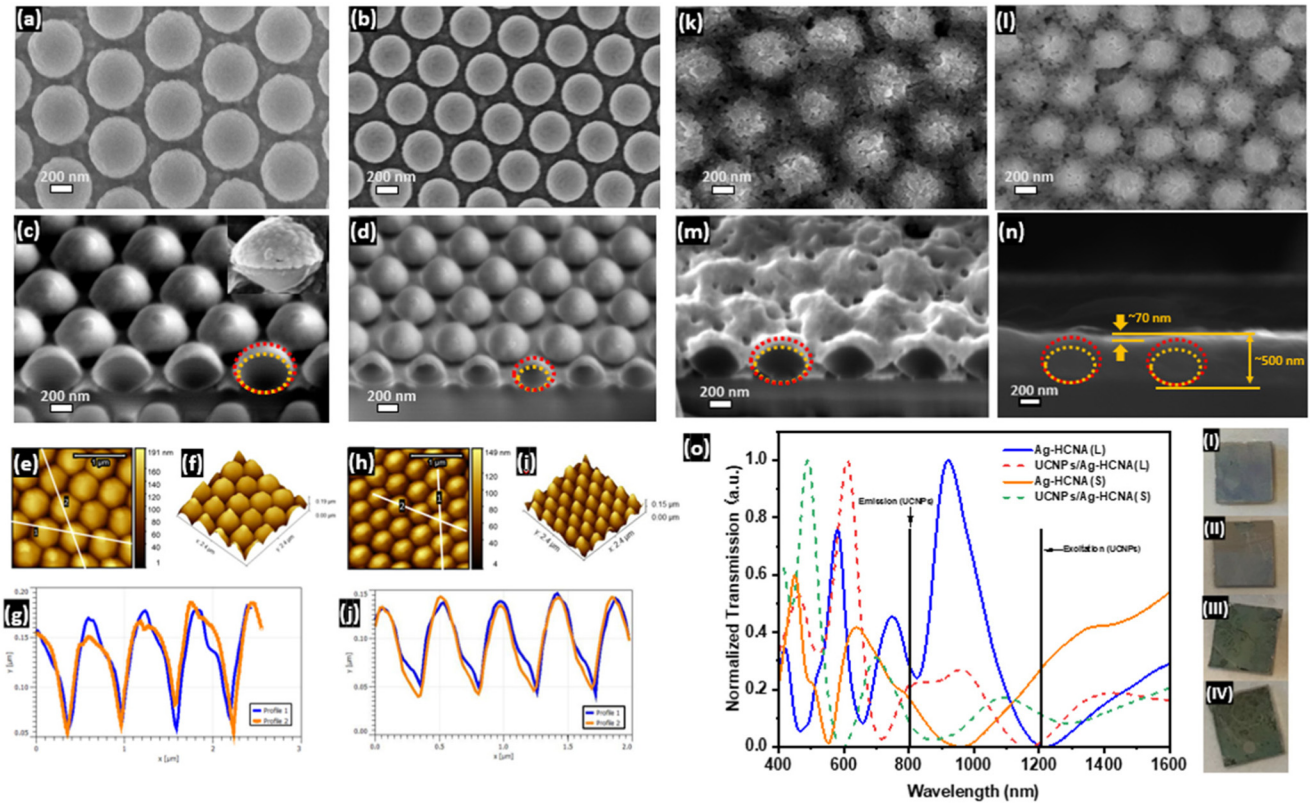

Fig. 2 Morphological characterization of UCNP-coated Ag-HCNA films. (a, b) SEM images of pristine (a) Ag-HCNA(L) and (b) Ag-HCNA(S) films. (c, d) SEM-FIB images of (c) Ag-HCNA(L) and (d) Ag-HCNA(S) films, cutting through the middle of individual Ag hemisphere caps. The inset in (c) shows a SEM image of a single Ag hemisphere cap. (e–h) AFM topological images of (e) Ag-HCNA(L) and (h) Ag-HCNA(S) films. (f) and (i) 3D profiles corresponding to (e) and (h), respectively. (g) and (j) Line profiles from the labels in (e) and (h), respectively. (k, l) SEM images of UCNP-coated PEGylated Ag-HCNA films: (k) UCNPs/Ag-HCNA(L) and (l) UCNPs/Ag-HCNA(S). (m) SEM-FIB image of UCNPs/Ag-HCNA(L), cutting through the middle of individual Ag hemisphere caps. (n) SEM cross-sectional (90° tilting) image of UCNPs/Ag-HCNA(L). (o) Transmission spectra of both types of Ag-HCNA films and the corresponding UCNPs/Ag-HCNA films. The insets (I–IV) show digital camera images of Ag-HCNA(L), UCNPs/Ag-HCNA(L), Ag-HCNA (S), and UCNPs/Ag-HCNA(S) films, respectively. The yellow dotted lines in (c), (d), (m), and (n) highlight the oval shaped PS spheres, while each red dotted line shows out the size of the Ag hemisphere caps.

longitudinal and transverse dimensions were reduced to 348 ± 17 nm and 274 ± 10 nm, respectively, while the resultant gap size between the Ag hemispherical cap and the hole was estimated to be ~98 ± 10 nm. Notably, under these processing conditions, the separation distance between adjacent Ag hemispherical caps was adjusted to ~75 ± 11 nm, comparable to that achieved using PS-617 beads. These findings also imply the reproducibility and reliability of the obtained Ag-HCNA film using a colloidal lithography nanofabrication method.

The deposition thickness of the Ag layer and the surface topographies of both types of Ag-HCNA films were further confirmed using AFM, as depicted in Fig. 2e–h and SI Fig. S6. The line profiles from the measured regions revealed a highly periodic arrangement of Ag hemispheres and holes, with an average Ag deposition thickness of approximately 50 nm across the scanned areas. These findings corroborate the observations obtained from SEM analysis.

Fig. 2k and i show the morphologies of UCNP-coated Ag-HCNAs. The thiol group from linear heterobifunctional SH-PEG-NH_2 ligands formed a strong bond with the Ag-HCNA film, forming a dielectric spacer layer over 5 nm. This effectively minimized non-radiative energy transfer and quenching between the Ag surface and the UCNPs. Besides, the amine groups on the opposite ends of the SH-PEG-NH_2 ligands served as anchoring sites for the PAA-DCNPs and enhanced the hydrophilicity of the PEGylated Ag-HCNA surface. To achieve a uniform coating and facilitate systematic investigation of plasmonic modulations on the UCNPs, the PAA-UNCPs were directly deposited onto the PEGylated Ag-HCNAs by drop-casting, forming an ~70 nm UCNP layer on top of the Ag-HCNAs (Fig. 2m and n). Notably, after coating with the UCNPs, the structure and periodicity of the Ag-HCNAs remained largely unchanged.

Fig. 2o shows the transmission spectra of two types of Ag-HCNAs before and after coating with the DCNPs. The pristine Ag-HCNAs, for both types, exhibited multiple transmission peaks and dips across the visible and NIR regions, attributed to the quadra-pole plasmonic modes arising from structural elements such as the holes and caps, and their coupled features on the Ag-HCNA substrate. Upon coating with the

UCNPs, both types of Ag-HCNA showed peak shifts and significant changes in the relative intensity of their peaks in the visible and NIR regions. Since there was no evidence suggesting that UCNP deposition degraded the array's order, we assume that the peak shifts and intensity changes are primarily attributable to the changes in the dielectric environment. Importantly, after UCNP coating, the transmission dip of UCNPs/Ag-HCNA(L) closely matched the extinction band of UCNPs at ~1208 nm, while the UCNPs/Ag-HCNA(S) exhibited overlap with the emission band of UCNPs at ~808 nm. As the transmission dip likely corresponds to the surface plasmon resonance of the nanostructured film, these strong spectral overlaps between the Ag-HCNAs and the coupled UCNPs are expected to significantly enhance the luminescence of UCNPs.

Luminescence enhancement results

The emission spectra of UCNPs on glass and on both types of Ag-HCNA films are shown in Fig. 3a. The emission peak at ~808 nm corresponds to the electronic transition ($^3H_4 \rightarrow {}^3H_6$) of Tm^{3+} ions within the UCNPs excited at 1208 nm, consistent with the emission spectrum observed in their aqueous form (Fig. 1g). Notably, a significant fluorescence enhancement was observed upon depositing UCNPs onto both types of Ag-HCNAs, with enhancements averaging 210-fold for Ag-HCNA (S) and 170-fold for Ag-HCNA(L), compared to the UCNPs on glass.

Fig. 3b shows the exceptional photostability of DCNPs on glass and on both types of Ag-HCNAs, even after long-time exposure to a NIR-II laser source. This was attributed to the intrinsic electronic configuration of emitter Tm^{3+} ions, wherein the electronic transitions of 4f electrons in the Tm^{3+} ions are localized and negligibly affected by the surrounding environment due to the shielding effect of the filled 5s and 5p sub-orbitals. The substantial enhancement of NIR UCL signals by Ag-HCNAs upon excitation within the biologically transparent NIR-II window, combined with the demonstrated photostability, implies the potential of integrating Ag-HCNAs with DCNPs as an ideal plasmonic platform for nanobiotechnology.

Fig. 3c shows a log–log plot illustrating the correlation between the fluorescence intensity of UCNPs and the excitation power on the glass, Ag-HCNA(S), and Ag-HCNA(L) films. The fluorescence intensity demonstrated a nearly quadratic dependence on the excitation power density, indicative of a typical 'two-photon' luminescence process, where two photons from excitation source are absorbed and converted into a single higher-energy emitting photon.[51] This observation supports the proposed energy transfer mechanism depicted in Fig. 1f.

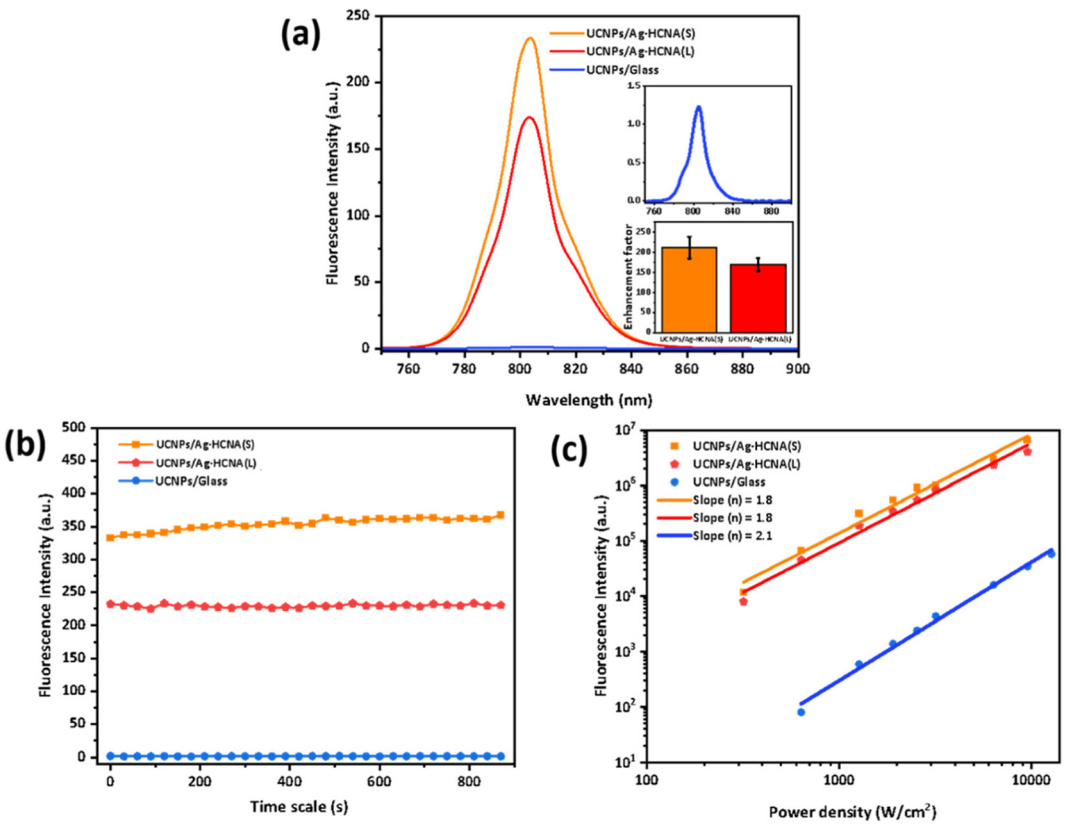

Fig. 3 UCL enhancement study of UCNP-coated Ag-HCNA films excited at 1208 nm. (a) PL spectra of UCNPs on a glass slide and Ag-HCNA films. Inset: (top) zoomed-in image of the PL spectra of UCNPs on a glass slide; (bottom) averaged fluorescence enhancement factor under emission at 808 nm calculated from the intensity ratio of UCNPs on Ag-HCNAs *versus* glass. (b) Fluorescence stability test. (c) Log–log plot of power density *versus* the fluorescence intensity of UCNPs on glass and on Ag-HCNAs.

Physical mechanism analysis

Fig. 4a and b present the simulated transmission spectra for Ag-HCNA(S) and Ag-HCNA(L), obtained using the three-dimensional finite-difference time-domain (FDTD) method with structural parameters from SI Table S1. The simulated spectra exhibit several main peaks that closely match the experimental data shown in Fig. 2o (blue and orange solid lines), indicating high periodicity and reproducibility for both array types. The excellent agreement in peak positions validates the accuracy of the structural modeling. However, minor discrepancies in intensity, such as that near 800 nm, arise from factors not considered in the ideal simulation, including surface roughness and realistic metal loss.

Fig. 4c and d show 3D FDTD modelling of the enhanced local *E*-field distribution across the surface of each Ag-HCNA type under a 1208 nm linear polarized beam directed perpendicularly to the array surface. Notably, the local *E*-fields varied at different positions along the Ag-HCNAs. For both types, a maximum local *E*-field enhancement of up to 5-fold was observed at the side edges of each hemispherical cap, while the regions between two adjacent hemispherical caps exhibited secondary strong local *E*-fields, varying from 3-fold to 5-fold enhancements. The excitation rate of Tm^{3+} ions within the UCNPs situated in these *E*-field-enhanced regions can be significantly accelerated, exhibiting a proportional relationship with the degree of *E*-field enhancement, as described by eqn (1):

$$\frac{r}{r_0} \propto \left(\frac{E}{E_0}\right)^{2n} \quad (1)$$

where 'r_0' and 'r' represent the original and accelerated excitation rates of sensitizer ions incorporated in the UCNPs and 'E_0' and 'E' denote the magnitudes of the incident *E*-field and the enhanced local *E*-field, respectively. The parameter 'n' signifies the number of photons required to excite electrons from the ground state to a higher energy state. In conventional one-photon lanthanide-induced DCL, 'n' is defined as 1.

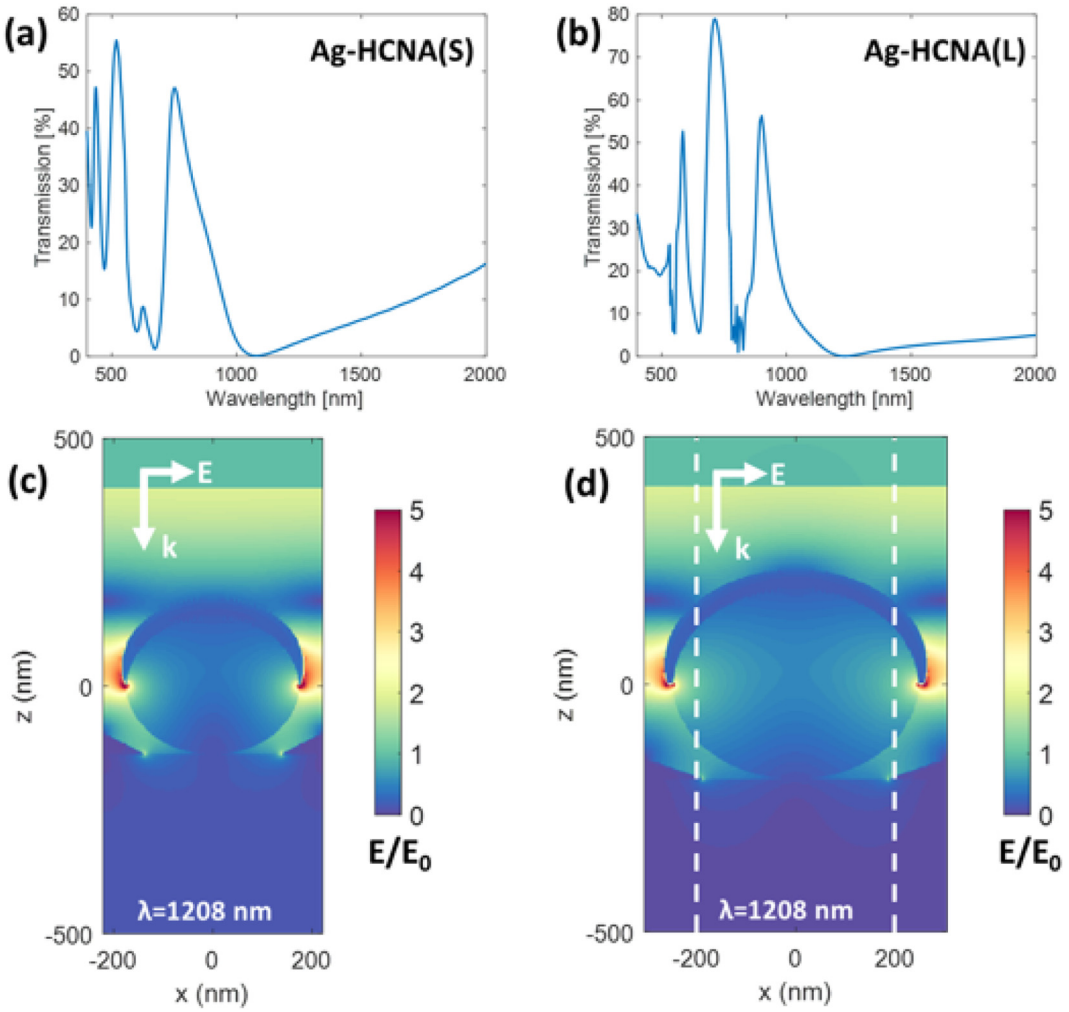

Fig. 4 Simulation of Ag-HCNA(S) and Ag-HCNA(L) using the 3D finite-difference time-domain (FDTD) method. (a, b) Simulated transmission spectra of (a) Ag-HCNA(S) and (b) Ag-HCNA(L). (c, d) Local *E*-field enhancement plot under a linearly polarized 1208 nm excitation beam. The white dashed circle in (d) indicates the position along the *x*-axis, where $x = \pm 200$ nm. '*E*' represents the *E*-field polarization and '*k*' denotes the wavevector. The unit bar in each *E*-field plot shows the amplitude of '*E*'.

Conversely, for the Tm^{3+}-induced UCL process, '*n*' is defined as 2, corresponding to a two-photon process. Consequently, local electric field enhancement by a factor of up to 5 can accelerate the excitation rate of Tm^{3+} ions by a maximum of 625-fold theoretically.

In the absence of other interactions, the NIR-UCL intensity from the Tm^{3+}-doped UCNPs under 1208 nm excitation can be enhanced by up to 625-fold. However, the competitive radiative and non-radiative decay rates of Tm^{3+}-induced 'one-photon' DCL, such as transitions ($^3H_5 \rightarrow {}^3H_6$ and $^3F_4 \rightarrow {}^3H_6$) of Tm^{3+}, may also be enhanced by the plasmonic characteristics of Ag-HCNAs. This enhancement can lead to faster depopulation of $^3H_5$ states, thereby suppressing UCL processes.

In addition to accelerating the excitation rate, the emission rate of UCNPs can be increased when they are positioned near metallic arrays. This enhancement arises from acceleration of the radiative decay rate of excited states *via* the Purcell effect through plasmonic confinement. Such an increase in the emission rate significantly contributes to the overall fluorescence enhancement. To further understand the role of emission rate enhancement, the fluorescence lifetimes at 808 nm from UCNPs on glass and Ag-HCNAs were measured, as shown in Fig. 5.

To analyze the excited-state lifetime of Tm^{3+}, the decay curves presented in Fig. 5a–c were obtained using a frequency-domain approach. In each measurement, the samples were excited at 1208 nm, and the emitted photons at 808 nm were collected. Both the excitation and emission beams were directed through mechanical choppers to produce a near-square-wave modulation response. This configuration enables the investigation of the population dynamics of the excited state under periodic excitation. Under square-wave modulation at a frequency ν over a single period $T = \nu^{-1}$, the temporal evolution of the emitting state was interpreted using a three-level model. The spectrometer integrates the signal over an integration time, corresponding to $\nu \cdot t_{int}$ modulation periods. When the two choppers are operated out of phase (blocking the emission while the sample is excited, and *vice versa*), the measured signal, denoted P_π, reflects the delayed emission dynamics. This signal is normalized against a reference measurement $P_* = \eta \cdot t_{int}$ obtained under identical integration conditions but without the choppers, where η represents the overall collection and detection efficiency. The ratio P_π/P_* is plotted as a function of modulation frequency on the *y*-axis in Fig. 5a–c. By analyzing the frequency-dependent behaviour of this ratio using eqn (1)–(6) from the SI, the excited-state lifetime of Tm^{3+} can be extracted, as the roll-off in the normalized signal with increasing frequency reflects the finite response time of the emitting state.

The measurement reveals that UCNPs on glass exhibit an intrinsically longer lifetime of ~41 μs, whereas UCNPs on Ag-HCNA(S) and Ag-HCNA(L) exhibit significantly shorter lifetimes of ~18 μs and 20 μs, respectively. Previous studies have shown that the fluorescence lifetime of lanthanide ions in a

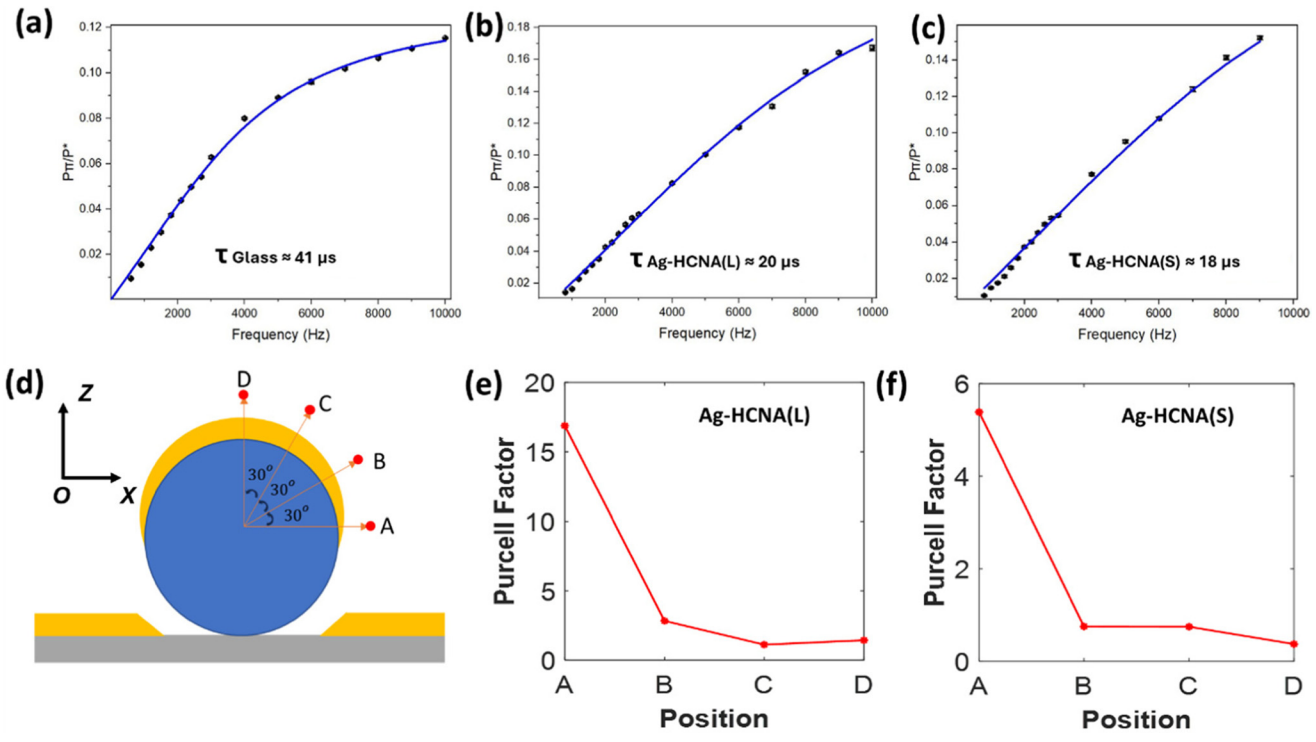

Fig. 5 Lifetime measurements and Purcell factor simulations of Tm^{3+}-induced NIR-UCL emission at 808 nm under 1208 nm excitation. (a–c) Lifetime plot and mono-exponential fit curve of (a) Tm^{3+}-doped UCNPs on glass, (b) Tm^{3+}-doped UCNPs on the Ag-HCNA(L) film, and (c) Tm^{3+}-doped DCNPs on the Ag-HCNA(S) film. (d–f) Purcell factor simulations for both types of Ag-HCNA structures. (d) Schematic illustration of Purcell factor modelling configuration. (e, f) Averaged Purcell factors *versus* positions for (e) Ag-HCNA(L) and (f) Ag-HCNA(S).

plasmonic cavity can be decomposed into two distinct emitter lifetimes, equivalent to a bi-exponential fit. In such cases, the longer lifetime is associated with uncoupled emitting ions, while the shorter lifetime corresponds to plasmonic-coupled ions.[28,29,40] However, in this study, UCNPs coupled with both types of Ag-HCNAs exhibit fluorescence lifetimes that can only be modelled using a mono-exponential fit, indicating uniformly shorter lifetimes. This observation can be attributed to the predominance of photons with faster decay rates, overshadowing those with longer decay rates that remain unaffected by the plasmonic effect. Consequently, the detection of photons with longer decay rates becomes negligible compared to the substantial number of photons with shorter decay rates.

When coupled with metallic arrays, both the radiative and non-radiative decay rates of Tm^{3+} ions can be increased. The increase in the radiative decay rate directly contributes to the enhanced fluorescence. However, a concurrent rise in the non-radiative decay rate leads to fluorescence quenching. Notably, by pre-coating a dielectric spacer layer ~5 nm thick over the surface of the Ag-HCNAs, the non-radiative decay rate can be significantly reduced.[28] Therefore, the spacer layer enabled a net emission enhancement of NIR-I UCL while minimizing the increase of the non-radiative decay rate.

Based on SI Fig. S4, it is assumed that multi-layer Tm^{3+}-doped UCNPs are uniformly deposited on both Ag-HCNA(L) and Ag-HCNA(S), forming a ~70 nm thick layer of DCNPs, which corresponds to approximately three layers of UCNPs. Given that the UCNPs are situated in regions with varying degrees of *E*-field enhancement, it can be inferred from SI Fig. 4a and b that ~25% of the total UCNPs on Ag-HCNA(S) experienced a local *E*-field enhancement ranging from 2-fold to 5-fold, while the remaining 75% experienced negligible *E*-field enhancement. For UCNPs on Ag-HCNA(L), it was estimated that only 15% of the total UCNPs experienced a local *E*-field enhancement within the same range, with 85% experiencing negligible enhancement. Among the UCNPs subjected to enhanced *E*-fields, the majority were within regions experiencing an ~2.5- to 3-fold enhancement.

Assuming an average local *E*-field enhancement of 2.5-fold and using the measured lifetimes of pristine UCNPs and plasmonic-modified UCNPs, the radiative decay rate enhancement was estimated to be ~5.4-fold for UCNPs on Ag-HCNA(S) and ~4.4-fold for UCNPs on Ag-HCNA(L). Correspondingly, applying eqn (8)–(13) from the SI yields an estimated quantum yield enhancement of approximately 2.3-fold for UCNPs on Ag-HCNA(S) and 2.1-fold for those on Ag-HCNA(L). When considering an average local *E*-field enhancement of 3-fold, the radiative decay rate enhancement was estimated to be approximately 2.6-fold for UCNPs on Ag-HCNA(S) and 2.1-fold for UCNPs on Ag-HCNA(L), with negligible changes in the corresponding quantum yield enhancement. Under these assumptions, the valid range for the quantum yield enhancement was between 1.1 and 2.3 for UCNPs on Ag-HCNA(S), and between 1 and 2.1 for UCNPs on Ag-HCNA(L). These results suggest that the local *E*-field enhancement, which accelerates 'two-photon' excitation processes, plays a primary role in enhancing the overall UCL signals from Tm^{3+}-doped UCNPs.

In Fig. 5d–f, the simulated Purcell factor for emitters situated close to the surfaces of both Ag-HCNA structures is illustrated. It is particularly noteworthy that the Purcell factor is higher near the edge of the Ag hemisphere cap, with Ag-HCNA (S) demonstrating a substantially larger Purcell factor compared to Ag-HCNA(L). Besides, the average Purcell factors across 4 selected regions are all higher for Ag-HCNA(S) compared to Ag-HCNA(L). This observation aligns well with the radiative decay rate enhancement of Tm-doped UCNPs on both types of Ag-HCNA, as detailed in Table S2. In practice, the measured Purcell factor represents an average value for emitters distributed across all surfaces of the structures, falling within the range of simulated values.

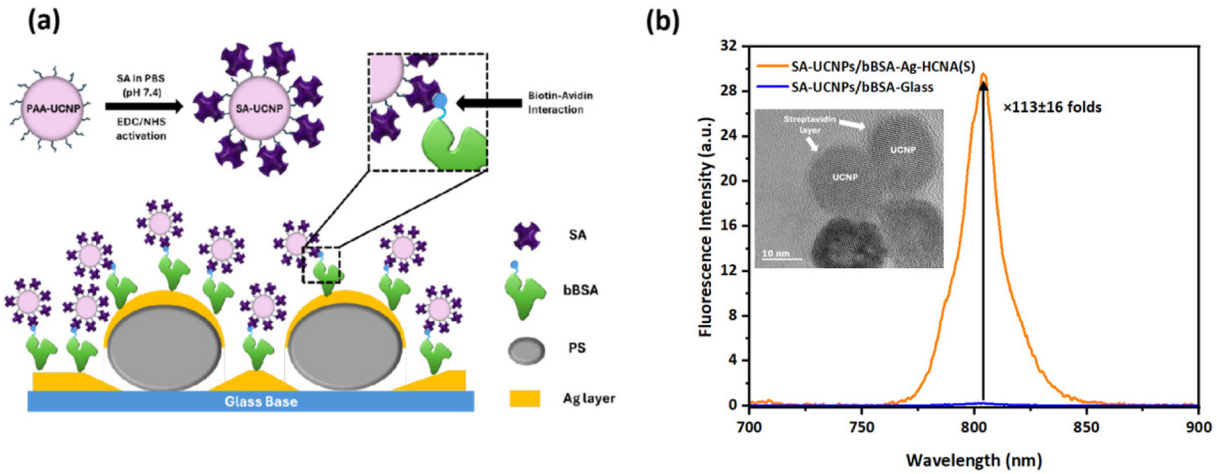

Fig. 6 Fluorescence enhancement study of a sub-monolayer of SA-UCNPs immobilized onto Ag-HCNA(S). (a) Scheme of sub-monolayer SA-UCNP coating on the Ag-HCNA substrate. (b) Fluorescence enhancement test using NIR-II excitation at 1208 nm. Inset: TEM morphological image of SA-UCNPs.

Model system for MEF-based immunoassays

In a practical MEF immunoassay nanoplatform, it is crucial for antibody-labelled fluorescent probes to establish a robust attachment to the protein-anchored plasmonic substrate *via* a self-assembled monolayer of molecular spacers, even after multiple washing steps.[41,52] The enhancement of UCL signals using Ag-HCNAs for potential applications in fluorescence immunoassays was further validated and is schematically illustrated in Fig. 6a. This study investigates the plasmonic effects of Ag-HCNA films on a sub-monolayer of streptavidin-functionalized Tm^{3+}-doped UCNPs immobilized through biotin–streptavidin interactions. A monolayer of bBSA was covalently bound to Ag-HCNAs due to the affinity between silver from the array film and the thiol groups from bBSA. Streptavidin was coated onto individual PAA-UCNPs *via* EDC–NHS chemistry, leveraging the interaction between carboxyl groups from PAA and amino groups from streptavidin. Subsequently, streptavidin-functionalized UCNPs were firmly immobilized on bBSA-coated Ag-HCNAs through biotin–avidin interactions, remaining stable even after multiple wash cycles. The inset in Fig. 6b shows individual UCNPs surrounded by an amorphous layer, confirming successful streptavidin functionalization. The PL spectra in Fig. 6b reveal that the near-infrared UCL signals from a sub-monolayer of UCNPs immobilized on glass are exceedingly weak, while UCNPs immobilized on Ag-HCNAs exhibit a pronounced UCL signal, with an average enhancement of 113-fold compared to UCNPs on glass. These preliminary results validate the potential of significantly amplifying weak NIR-UCL signals from sub-monolayer UCNPs, which contain a much lower concentration of UCNPs compared to multi-layer configurations. For practical ELISA measurements, we aim to continually improve the limit of detection by measuring fluorescence signals from UCNP concentrations as low as pg L^{-1}. With Ag-HCNAs serving as signal amplifiers, we are confident in achieving this objective.

Conclusion

This study presents a significant advancement in utilizing plasmonic-enhanced NIR-II responsive UCNPs. By coupling Tm^{3+}-doped $NaYF_4$ UCNPs with PEGylated Ag-HCNAs through drop-casting, a substantial enhancement of more than 240-fold was observed in Tm^{3+}-induced UCL at 808 nm under 1208 nm laser excitation, compared to pristine UCNPs on glass substrates. The underlying enhancement mechanisms were investigated using 3D-FDTD simulations at 1208 nm excitation, which revealed localised electromagnetic 'hot spots' at the edges of hemispherical caps. Lifetime measurements further indicated that the dominant contribution to the observed UCL enhancement arises from local electric field amplification, which exhibits a quadratic dependence on the excitation power. In contrast, the contribution of emission enhancement plays a secondary role. Moreover, the potential of Ag-HCNA-based UCL amplification for fluorescence immunoassay applications was validated by immobilizing a sub-monolayer of streptavidin-functionalized UCNPs on biotinylated bovine serum albumin (bBSA) pre-grafted array substrates. A remarkable enhancement up to 113-fold relative to traditional glass substrates was achieved, demonstrating the capability of this approach for substantially amplifying weak NIR-UCL signals in plasmonic-enhanced UCL immunoassay platforms. The designed plasmonic-enhanced UCL platform, featuring excitation within the biologically transparent NIR-II window and emission in the NIR-I region, offers distinct technical and economic advantages. These include reduced biological autofluorescence, improved signal-to-noise performance and cost-effective detection of NIR-I emission using conventional silicon-based detectors. In summary, the integration of NIR-I emitting UCNPs with plasmonic nanoarrays provides a powerful and practical sensing platform with strong potential to advance the field of fluorescence-based immunoassay technologies.

Conflicts of interest

The authors have no conflicts to disclose.

Data availability

The authors confirm that the data supporting the findings of this study are available within the article and its supplementary information (SI). Supplementary information is available. See DOI: https://doi.org/10.1039/d6nr00068a.

Acknowledgements

F. X. acknowledges the Henry Royce Institute through EPSRC grant EP/R00661X/1. The authors acknowledge the use of characterization facilities within the Harvey Flower Electron Microscopy Suite at the Department of Materials, Imperial College London.

References

1 S. M. Fothergill, C. Joyce and F. Xie, Metal enhanced fluorescence biosensing: From ultra-violet towards second near-infrared window, *Nanoscale*, 2018, **10**(45), 20914–20929.
2 E. M. Goldys, Plasmon-enhanced fluorescence near metallic nanostructures: biochemical applications, *Appl. Phys. A*, 2007, **89**(2), 265–271.
3 Y. Hang, J. Boryczka and N. Wu, Visible-light and near-infrared fluorescence and surface-enhanced Raman scattering point-of-care sensing and bio-imaging: A review, *Chem. Soc. Rev.*, 2022, **51**(1), 329–375.
4 I. S. Martins, *et al.*, Measurement of tissue optical properties in a wide spectral range: A review, *Biomed. Opt. Express*, 2022, **14**(1), 249–298.

5 V. V. Tuchin, Tissue optics and photonics: Light–tissue interaction, *J. Biomed. Photonics Eng.*, 2015, **1**(2), 98–134.
6 C. Chen, *et al.*, Activatable fluorescence probes for "turn-on" and ratiometric biosensing and bioimaging: From NIR-I to NIR-II, *Bioconjugate Chem.*, 2020, **31**(2), 276–292.
7 S. Li, *et al.*, Recent progresses in NIR-I/II fluorescence imaging for surgical navigation, *Front. Bioeng. Biotechnol.*, 2021, **9**, 768698.
8 Z. Lei and F. Zhang, Molecular engineering of NIR–II fluorophores for improved biomedical detection, *Angew. Chem., Int. Ed.*, 2021, **60**(30), 16294–16308.
9 J. Cao, *et al.*, Recent progress in NIR-II contrast agent for biological imaging, *Front. Bioeng. Biotechnol.*, 2020, **7**, 487.
10 A. L. Antaris, *et al.*, A small-molecule dye for NIR-II imaging, *Nat. Mater.*, 2016, **15**(2), 235–242.
11 L. Li, *et al.*, A short review on NIR-II organic small molecule dyes, *Dyes Pigm.*, 2020, **183**, 108756.
12 L. L. Chen, *et al.*, Near-infrared-II quantum dots for in vivo imaging and cancer therapy, *Small*, 2022, **18**(8), 2104567.
13 S. Xu, J. Cui and L. Wang, Recent developments of low-toxicity NIR II quantum dots for sensing and bioimaging, *TrAC, Trends Anal. Chem.*, 2016, **80**, 149–155.
14 J. Pan, F. Li and J. H. Choi, Single-walled carbon nanotubes as optical probes for bio-sensing and imaging, *J. Mater. Chem. B*, 2017, **5**(32), 6511–6522.
15 G. Hong and H. Dai, *In vivo fluorescence imaging in the second near-infrared window using carbon nanotubes*, In Vivo Fluorescence Imaging: Methods and Protocols, 2016, 167–181.
16 S. Ding, *et al.*, Recent progress in NIR-II emitting lanthanide-based nanoparticles and their biological applications, *J. Rare Earths*, 2020, **38**(5), 451–463.
17 X. Ge, R. Wei and L. Sun, Lanthanide nanoparticles with efficient near-infrared-II emission for biological applications, *J. Mater. Chem. B*, 2020, **8**(45), 10257–10270.
18 Z. Yi, *et al.*, Lanthanide-activated nanoparticles: A toolbox for bioimaging, therapeutics, and neuromodulation, *Acc. Chem. Res.*, 2020, **53**(11), 2692–2704.
19 Y. Liu, K. Ai and L. Lu, Designing lanthanide-doped nanocrystals with both up-and down-conversion luminescence for anti-counterfeiting, *Nanoscale*, 2011, **3**(11), 4804–4810.
20 A. Nadort, J. Zhao and E. M. Goldys, Lanthanide upconversion luminescence at the nanoscale: Fundamentals and optical properties, *Nanoscale*, 2016, **8**(27), 13099–13130.
21 M. V. DaCosta, *et al.*, Lanthanide upconversion nanoparticles and applications in bioassays and bioimaging: A review, *Anal. Chim. Acta*, 2014, **832**, 1–33.
22 J. Yan, *et al.*, Progress in light-responsive lanthanide nanoparticles toward deep tumor theranostics, *Adv. Funct. Mater.*, 2021, **31**(42), 2104325.
23 F. Wang, R. Deng and X. Liu, Preparation of core-shell $NaGdF_4$ nanoparticles doped with luminescent lanthanide ions to be used as upconversion-based probes, *Nat. Protoc.*, 2014, **9**(7), 1634–1644.
24 X. Lei, *et al.*, Intense near-infrared-II luminescence from $NaCeF_4$: Er/Yb nanoprobes for in vitro bioassay and in vivo bioimaging, *Chem. Sci.*, 2018, **9**(20), 4682–4688.
25 Y. Song, *et al.*, Deep learning fluorescence imaging of visible to NIR-II based on modulated multimode emissions lanthanide nanocrystals, *Adv. Funct. Mater.*, 2022, **32**(45), 2206802.
26 A. A. Ansari, *et al.*, Luminescent lanthanide nanocomposites in thermometry: Chemistry of dopant ions and host matrices, *Coord. Chem. Rev.*, 2021, **444**, 214040.
27 H. Yang, *et al.*, Preparation and properties of Nd^{3+} doped Gd_2O_3 near-infrared phosphor, *Ceram. Int.*, 2021, **47**(6), 8510–8517.
28 J. Xu, *et al.*, Plasmonic-enhanced NIR-II downconversion fluorescence beyond 1500 nm from core–shell–shell lanthanide nanoparticles, *Adv. Opt. Mater.*, 2023, **11**(19), 2300477.
29 J. Xu, *et al.*, Remarkable plasmonic enhanced luminescence of Ce^{3+} doped lanthanide downconversion nanoparticles in NIR-II window by silver hole–cap nanoarrays, *Adv. Opt. Mater.*, 2024, **12**(30), 2400660.
30 S. Bi, *et al.*, NIR-II responsive upconversion nanoprobe with simultaneously enhanced single-band red luminescence and phase/size control for bioimaging and photodynamic therapy, *Adv. Mater.*, 2023, **35**(7), 2207038.
31 Y. Li, *et al.*, Engineered lanthanide-doped upconversion nanoparticles for biosensing and bioimaging application, *Microchim. Acta*, 2022, **189**(3), 109.
32 Y. Guo, *et al.*, In vivo NIR-II fluorescence lifetime imaging of whole–body vascular using high quantum yield lanthanide-doped nanoparticles, *Small*, 2023, **19**(35), 2300392.
33 A. M. Smith, M. C. Mancini and S. Nie, Second window for in vivo imaging, *Nat. Nanotechnol.*, 2009, **4**(11), 710–711.
34 S. Derom, *et al.*, Metal enhanced fluorescence in rare earth doped plasmonic core–shell nanoparticles, *Nanotechnology*, 2013, **24**(49), 495704.
35 K. Aslan, *et al.*, Metal-enhanced fluorescence: an emerging tool in biotechnology, *Curr. Opin. Biotechnol.*, 2005, **16**(1), 55–62.
36 M. Saboktakin, *et al.*, Metal-enhanced upconversion luminescence tunable through metal nanoparticle–nanophosphor separation, *ACS Nano*, 2012, **6**(10), 8758–8766.
37 Y. Jeong, *et al.*, Metal enhanced fluorescence (MEF) for biosensors: General approaches and a review of recent developments, *Biosens. Bioelectron.*, 2018, **111**, 102–116.
38 K. Dhanasiwawong, *et al.*, Preparation of 2D periodic nanopatterned arrays through vertical vibration-assisted convective deposition for application in metal-enhanced fluorescence, *Processes*, 2022, **10**(2), 202.
39 M. Saboktakin, *et al.*, Plasmonic enhancement of nanophosphor upconversion luminescence in Au nanohole arrays, *ACS Nano*, 2013, **7**(8), 7186–7192.
40 F. Xie, *et al.*, Nanoscale control of Ag nanostructures for plasmonic fluorescence enhancement of near-infrared dyes, *Nano Res.*, 2013, **6**, 496–510.
41 Y. Li, *et al.*, NIR-II emitting rare-earth nanoparticles for a lateral flow immunoassay in hemolysis, *Sens. Actuators, B*, 2021, **345**, 130380.

42 Z. Song, *et al.*, NIR-II fluorescent nanoprobe-labeled lateral flow biosensing platform: A high-performance point-of-care testing for carcinoembryonic antigen, *Biosens. Bioelectron.*, 2023, **224**, 115063.
43 Z. Song, *et al.*, NIR-II fluorescence lateral flow immunosensor based on efficient energy transfer probe for point-of-care testing of tumor biomarkers, *Chin. Chem. Lett.*, 2024, 109834.
44 W. Kong, *et al.*, A general strategy for ligand exchange on upconversion nanoparticles, *Inorg. Chem.*, 2017, **56**(2), 872–877.
45 I. Theodorou, *et al.*, Significant metal enhanced fluorescence of Ag 2 S quantum dots in the second near-infrared window, *Nanoscale*, 2016, **8**(26), 12869–12873.
46 J. S. Pang, *et al.*, Tunable three-dimensional plasmonic arrays for large near-infrared fluorescence enhancement, *ACS Appl. Mater. Interfaces*, 2019, **11**(26), 23083–23092.
47 J. Pang, *et al.*, Gold nanodisc arrays as near infrared metal-enhanced fluorescence platforms with tuneable enhancement factors, *J. Mater. Chem. C*, 2017, **5**(4), 917–925.
48 J. Xu, *et al.*, Significant quantum yield enhancement for near infrared fluorescence dyes by silica templated silver nanorods, *Appl. Phys. Rev.*, 2022, **9**(3), 031406.
49 N. A. Güsken, *et al.*, Emission enhancement of erbium in a reverse nanofocusing waveguide, *Nat. Commun.*, 2023, **14**(1), 2719.
50 D. Darvill, *et al.*, Breaking the symmetry of nanosphere lithography with anisotropic plasma etching induced by temperature gradients, *Nanoscale Adv.*, 2021, **3**(2), 359–369.
51 D. M. Wu, *et al.*, Plasmon-enhanced upconversion, *J. Phys. Chem. Lett.*, 2014, **5**(22), 4020–4031.
52 R. Chen, *et al.*, NIR-II emissive lateral flow immunoassay for accurate determination of tumor marker in hemolysis, *Sens. Actuators, B*, 2021, **328**, 129050.